

# Radiacoustic imaging

Yifei Xu¹ & Shawn Liangzhong Xiang **®** <sup>1,2,3</sup> ⊠

#### **Abstract**

Ultrasound waves can be generated by various radiation sources, including X-rays, protons, electrons and electrical fields, through the rapid thermal expansions and contractions that occur when materials absorb deposited radiation energies. The ultrasound waves, which we refer to as 'radiacoustic waves', can be detected for imaging purposes. Radiacoustic imaging offers new imaging contrasts beyond traditional pulse–echo ultrasound. This Perspective provides an analysis of progress in radiacoustic imaging in recent years, focusing on biomedical and materials science applications. We explore the mechanisms behind radiacoustic imaging, highlight its current uses and challenges, and discuss potential advances to improve the effectiveness of radiacoustic imaging technologies across different fields.

#### **Sections**

Introduction

Principle of RAI

**Technology development** 

RAI via X-ray excitation

RAI via proton excitation

RAI via electron excitation

RAI via pulsed electrical field

RAI and its applications in materials science

Outlook

<sup>1</sup>Department of Biomedical Engineering, University of California Irvine, Irvine, CA, USA. <sup>2</sup>Department of Radiological Sciences, University of California Irvine, Irvine, CA, USA. <sup>3</sup>Beckman Laser Institute & Medical Clinic, University of California Irvine, Irvine, CA, USA. ⊠e-mail: liangzhx@hs.uci.edu

#### Introduction

Ultrasound is one the most widely used medical imaging modalities worldwide, offering real-time imaging of deep tissues<sup>1</sup>, organs<sup>2</sup> and blood flow<sup>3,4</sup>. However, conventional pulse–echo ultrasound can suffer from limited contrast, which can impede detailed diagnostic assessment<sup>5</sup>. To address this limitation, researchers have explored alternative energy sources to generate ultrasound signals, which provide richer contrast and more functional information. One such development is radiacoustic imaging (RAI), which uses energy sources such as X-rays<sup>6-10</sup>, protons<sup>11-17</sup>, electrons<sup>18,19</sup>, lasers<sup>5,20-26</sup> and electrical fields<sup>27-29</sup> to generate ultrasound waves through rapid thermal expansions and contractions in materials. This process uses either ionizing (X-ray, proton, electron) or non-ionizing (laser, or electrical field) forms of pulsed energy, often at microsecond scales or shorter<sup>30</sup> (Table 1), resulting in new types of imaging modalities.

Unlike conventional ultrasound, which forms images based on reflected echoes from impedance mismatches, RAI constructs images from the initial pressure rise generated by absorbed energy<sup>31</sup>. This fundamentally different approach enables the capture of image contrast driven by variations in material absorption properties, opening the door to new applications. For instance, RAI enables 3D X-ray absorption-based imaging from a single projection, surpassing conventional computed tomography capabilities<sup>10</sup>. It also allows real-time, in vivo monitoring of radiation dose deposition during radiotherapy<sup>11,18,19,32,33</sup>.

Much of the literature deals with laser-induced photoacoustic imaging<sup>5,26,31,34-40</sup>. Among the energy sources used for RAI, laser beams have emerged as particularly powerful for generating ultrasound, especially in the visible and near-infrared spectrum, which enables deep tissue penetration<sup>41,42</sup>. Laser-induced photoacoustic imaging is highly effective for visualizing microvasculature – structures that are difficult to detect with traditional ultrasound owing to the low echogenicity of small vessels<sup>43</sup>. Furthermore, by using spectroscopic measurements at multiple wavelengths, this technique can differentiate between oxyhaemoglobin and deoxyhaemoglobin to quantify blood oxygen saturation, providing functional information inaccessible to conventional ultrasound<sup>44</sup>.

The discussion in this Perspective instead focuses on the emerging applications of RAI using other radiation sources: X-rays, protons, electrons and electric fields. These advanced modalities may transform fields including medical imaging and therapeutic monitoring, industrial inspection and material characterization. We first discuss the principle behind RAI, before outlining how technology has developed in recent years, and then reviewing each of the radiation sources in turn. Finally, we outline applications in materials science and future directions.

## **Principle of RAI**

RAI can be intuitively understood by analogy to lightning and thunder. Just as a lightning strike rapidly heats the air, causing a pressure wave (thunder) that reveals both the location and intensity of the strike, RAI uses ultrashort radiation pulses to generate detectable acoustic signals in tissue or other material. The radiation pulses produce a slight temperature rise (typically less than a millikelvin), which, despite being minimal, is sufficient to induce thermoelastic expansion and generate ultrasound waves. For instance, in soft tissue, a temperature increase of 1 mK can produce a pressure rise of 800 Pa, well above the detection threshold of standard ultrasound transducers<sup>5</sup>. This process of excitation and detection allows precise localization of radiation interactions within the body, analogous to calculating the distance to a lightning strike based on the delay between light and sound.

The underlying mechanism involves a rapid sequence of microscopic processes: energy absorption by ionizing radiation, transient thermal confinement, and the generation of pressure waves through thermoelastic expansion. When the radiation pulse duration is shorter than the thermal and stress relaxation timescales, heat remains localized, leading to a strong acoustic response. Here, thermal confinement time  $(\tau_{th})$  refers to the time it takes for heat to begin diffusing out of the region where energy has been deposited. It is given by  $\tau_{\text{th}} \approx \frac{d^2}{4\alpha}$ , where d is the characteristic size of the heated region (which partly determines the spatial resolution of RAI), and  $\alpha$  is the thermal diffusivity of the tissue (typically about  $1.4 \times 10^{-7}$  m<sup>2</sup> s<sup>-1</sup> for soft tissue). For example, to achieve a 3-mm imaging resolution, the radiation pulse duration should be shorter than 16  $\mu$ s, a condition that is typically met in most cases. The amplitude of the resulting wave is determined by the Grüneisen parameter, linking thermal energy to pressure. These signals can be reconstructed into spatial dose maps, enabling real-time, in vivo imaging of radiation deposition.

The radiacoustic effect can be described by the following wave equation <sup>5,25,26</sup>,

$$\left(\nabla^2 - \frac{1}{v_s^2} \frac{\partial^2}{\partial t^2}\right) p(\mathbf{r}, t) = -\frac{\beta}{C_p} \frac{\partial H(\mathbf{r}, t)}{\partial t}$$
(1)

where p is the pressure as a function of position ( $\mathbf{r}$ ) and time (t),  $v_s$  is the speed of sound in the medium,  $\beta$  is the coefficient of volume expansion,  $C_p$  is the specific heat capacity at constant pressure and H is the heating function with respect to position and time. The equation is driven by the first temporal derivative of the heating function itself; thus time-invariant heating does not produce a radiacoustic signal. The solution to equation (1) is given by<sup>31</sup>:

Table 1 | Radiacoustic imaging with different radiation sources

Excitation source	Pulse duration	Repetition rate	Dose per pulse	Resolution	Depth	Speed
X-ray	~5 µs for therapy	~100 Hz	~1mGy (ref. 57)	~mm	>10 cm	~30 fps depending on the average number of pulses
	~50 ns for imaging	~10 Hz	~0.03 mGy (ref. 6)	Sub-mm	Several cm	<10 fps limited by pulse repetition period
Proton	~10 µs	~750–1,000 Hz	~20 mGy depending on the energy <sup>61</sup>	~mm	>10 cm	>30 fps depending on the averages
Electron	~1µs	~120 Hz	~Gy for FLASH <sup>18</sup>	~mm	Several cm	>100 fps for individual pulse
Electrical field	~100ns	~Hz-kHz	60 V cm <sup>-1</sup> to 10 kV cm <sup>-1</sup> (ref. 27)	Sub-mm	Several cm	>75 fps depending on the averages

fps, frames per second.

$$p(\mathbf{r},t) = \frac{\Gamma}{4\pi c} \frac{\partial}{\partial t} \left( \frac{1}{vt} \int_{S(\mathbf{r}',t)} H(\mathbf{r}') dS'(t) \right); |\mathbf{r} - \mathbf{r}'| = vt,$$
 (2)

where S'(t) represents a spherical surface centred at a detector (located at  $\mathbf{r}$ ) with radius  $v_s t$ , and  $\Gamma$  represents the Gruneisen coefficient.

The inverse problem corresponding to RAI is to obtain a 3D map of energy deposition ( $\tilde{H}(\mathbf{r})$ ) from a set of boundaries measurements  $p(\mathbf{r}_0, t)$  made at detectors located at  $\mathbf{r}_0$  on the detector grid  $S_0$ . A universal back-projection algorithm can be used for the image reconstruction<sup>45</sup>, which is given by:

$$\tilde{p}_{0}(\mathbf{r}) = \Gamma \tilde{H}(\mathbf{r}) = \int_{\mathbf{S}_{0}} b \left( \mathbf{r}_{0}, \ t = \frac{|\mathbf{r}_{0} - \mathbf{r}|}{v} \right) \frac{\mathrm{d}\Omega}{\Omega}$$
(3)

where the back-projection term  $b(\mathbf{r}_0,t)=2p(\mathbf{r}_0,t)-2t$   $\frac{\mathrm{d}p(\mathbf{r}_0,t)}{\mathrm{d}t}$ . A single detector reveals that the dose deposition lies somewhere along a circular path. By adding a second detector, the deposition position is narrowed down further, and with three detectors, the location is pinpointed precisely. In practice, one goes beyond just three detectors and uses hundreds to map the radiation beam in three dimensions, providing a detailed 3D visualization of the radiation dose deposition within the material 46. Other image reconstruction algorithms, such as time reversal 47,48, model-based approaches 49,50 and deep learning 11,51, can also be used for RAI reconstruction.

A direct relationship between the initial acoustic pressure and the radiation dose deposition can be expressed as  $^{33,52}$ 

$$p_{0}(r) = \Gamma \eta_{\rm rh} \rho D_{\rm p}(r) \tag{4}$$

Here  $\rho$  is the density, which along with  $\Gamma$  relates to the material characteristics.  $\eta_{\rm th}$  denotes radiacoustic signal conversion efficiency, which quantifies how efficiently absorbed energy (radiation pulses) is converted into an initial pressure rise that generates an acoustic signal, and  $D_{\rm p}({\bf r}) = D_{\bf r}({\bf r},t)\tau_{\rm p}$ , where  $D_{\bf r}({\bf r},t)$  is the local energy deposition due to a single electron pulse with a pulse duration of  $\tau_{\rm p}$ . Consequently, the pixel intensity within the RAI image is related to the radiation dose deposition, providing essential information about the location and amount of radiation dose deposited in the material.

#### Technology development

The progress of RAI for 3D dose mapping has been remarkable, advancing from a theoretical concept<sup>53</sup> to clinical patient testing<sup>54</sup> within just a decade.

The development of the RAI technology is largely driven by its intended clinical applications. For localizing the Bragg peak, a single-element transducer was commonly used in early experiments 55,56. Other studies focused on detecting acoustic signals generated by various radiation sources, using large, single-element ultrasound transducers 6,13,57. These foundational efforts established the basis for developing more sensitive detectors and advanced pre-amplification systems. An important technical improvement was the ability to detect single-pulse X-ray 58 and single-pulse proton 55 signals without averaging, enabling real-time localization of the Bragg peak during proton therapy (Fig. 1a) and potentially supporting future tracking of pencil beam scanning.

To image both dosimetry information and anatomical structures, researchers transitioned from using single-point detection to 2D imaging using linear ultrasound arrays<sup>17,59-62</sup> (Fig. 1b), which eliminated the need for mechanical scanning. In certain cases,

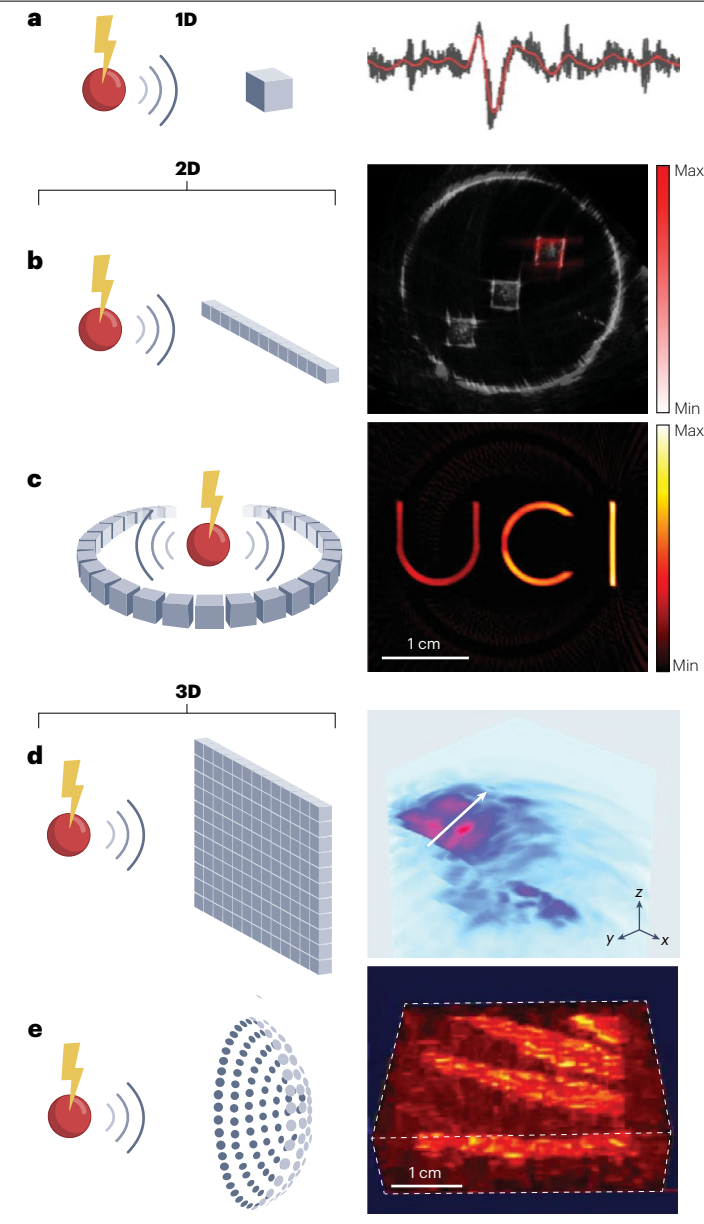


**Fig. 1**| **Transducer configurations for radiacoustic imaging (RAI), with corresponding signals and images. a**, A single transducer was used to detect radiacoustic waves for localizing the Bragg peak during proton therapy. **b**, A linear array was used to visualize the photon beam during radiotherapy, overlaid with pulse and echo ultrasound. **c**, Occasionally, a ring array has been used for diagnostic imaging. **d**, **e**, For 3D RAI, either a matrix array or a spherical array can be used, for applications such as electron therapy monitoring (part **d**) and 3D bone imaging (part **e**). Part **a** adapted with permission from ref. 55, IOP. Part **b** adapted with permission from ref. 59, AAAS. Part **c** adapted from ref. 64, CC BY 4.0. Part **d** adapted with permission from ref. 18, IOP. Part **e** adapted with permission from ref. 67, IEEE.

circular ultrasound arrays have been used to demonstrate proof of concept <sup>63,64</sup> (Fig. 1c).

When a 3D dose map is desired, matrix arrays are required 11,16,18,51,54,65,66 (Fig. 1d). These arrays have been validated through both simulation and experimental studies, demonstrating their

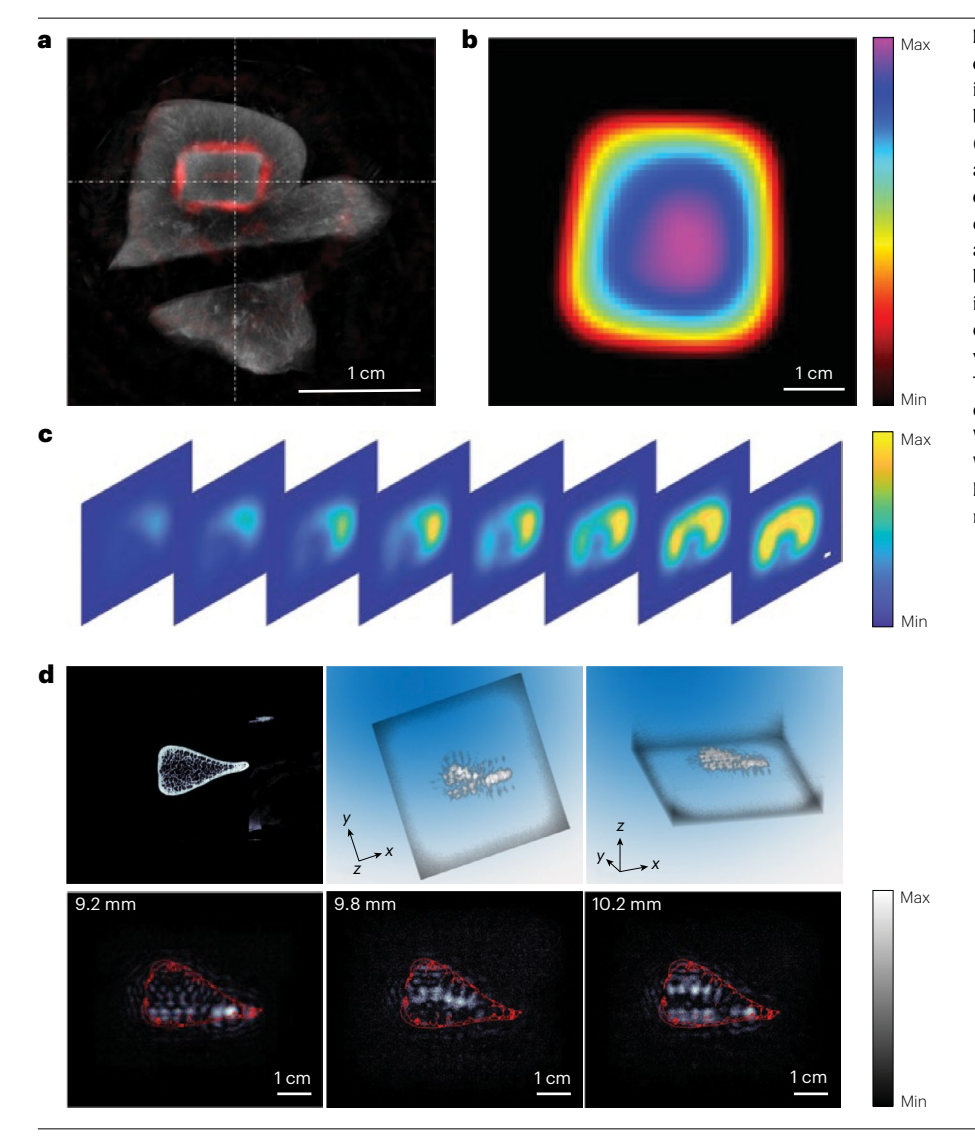


Fig. 2 | Radiacoustic imaging (RAI) via X-ray excitation. a, Dual-modality RAI and ultrasound imaging provide complementary information on both the radiation beam (red) and treatment target (grev), **b**. Map of dosage of a therapeutic X-ray attained from model-based image reconstruction. c, RAI allows real-time monitoring of radiation dose deposition during radiotherapy. The series of images are taken at different X-ray angles. d, Imaging of bone samples<sup>10</sup> using microcomputed tomography is shown in the upper left; 3D X-ray-induced acoustic computed tomography (XACT) images from different viewing angles are displayed in the upper right. The bottom panels present XACT images at various depths. Part a adapted with permission from ref. 77, Wiley. Part b adapted with permission from ref. 33, Wiley. Part c adapted from ref. 54, Springer Nature Limited. Part d adapted with permission from ref. 10. AAAS.

capability to reconstruct volumetric dose distributions. Furthermore, spherical arrays (Fig. 1e) have been proposed to improve lateral resolution in 3D imaging, with promising applications in bone  $^{32,67}$  and breast imaging  $^{68}$ .

Artificial intelligence (AI) may play an important role in enhancing RAI by using deep learning to denoise signals<sup>69</sup> and address the limited-view problem<sup>11,51,70,71</sup>. AI-driven denoising improves image clarity by filtering out noise using general deep inception convolutional neural networks trained on extensive radiacoustic datasets<sup>69</sup>. This enhancement not only improves image quality but also enables RAI with fewer radiation pulses and faster data acquisition, which aids in reducing patient exposure and increasing imaging speed. Furthermore, AI algorithms effectively address the limited-view challenge by reconstructing complete 3D images from sparse data. To tackle this issue in RAI, a deep learning method incorporating a two-stage 'recon–enhance' strategy has been developed<sup>51</sup>. In the 'recon' stage, a transformer-based network is designed to reconstruct initial pressure maps from radiofrequency signals. This network undergoes a

hybrid supervised training regime, initially trained under supervision using iteratively reconstructed pressure maps, then fine-tuned through transfer learning and self-supervision based on data fidelity constraints. During the 'enhance' stage, a 3D U-Net is used to further improve image quality, supervised by the ground-truth pressure maps. The enhanced images from this stage are subsequently converted into dose maps for radiotherapy monitoring.

In RAI, axial resolution depends on the acoustic time of flight, which is influenced by the pulse duration of the radiation source and the size of the absorption target, depending on whether time or spatial constraints are more critical <sup>30,72</sup>. Meanwhile, lateral resolution is determined by the size of the detector element. Quantitatively, both axial and lateral resolutions are defined by the full-width at half-maximum (FWHM) of the system's response to a point target, known as the point spread function<sup>3</sup>. The typical resolution of RAI for radiotherapy is of the order of millimetres, primarily determined by the pulse duration of the radiation beam and the beam size, and the material properties. Microscopic RAI can achieve lateral resolution at the subcellular or cellular

level, ranging from a few hundred nanometres to several micrometres, by focusing the radiation beam, although imaging depth is limited by radiation diffusion in the material <sup>14</sup>.

## **RAI** via X-ray excitation

An early form of RAI was X-ray-induced acoustic computed tomography (XACT) $^{53}$ , which was explored for in vivo dosimetry during radiotherapy. In a decade, RAI, in the form of XACT, has evolved from a new concept to being studied for dosimetry in patients. From a technical perspective, XACT offers several advantages as a complement to conventional radiation dosimeters. These unique benefits and its compatibility with ultrasonography enable XACT to be integrated into a dual-modality imaging system, providing both in vivo dosimetry and tumour motion management capabilities unmatched by any other imaging technology. Recently, it also shows the potential to be an alternative to conventional computed tomography that does not require gantry rotation  $^{6,10,68}$ .

#### In vivo dosimetry for photon therapy

Mega-electronvolt X-ray photon therapy is widely used in radiotherapy<sup>73,74</sup>. RAI that uses these photons as a source has demonstrated potential for real-time dose monitoring directly on patients<sup>27,32,33,54,58,75-77</sup>. This in vivo dosimetry capability enhances treatment precision by minimizing damage to healthy tissues, reducing treatment margins and improving quality assurance.

Evidence of the effectiveness of XACT has been demonstrated by using an X-ray beam to image phantoms made of yeal livers and fat,

indicating the ability of XACT to detail the position and distribution of radiation dose<sup>77</sup> (Fig. 2a). These abilities are needed for image-guided radiation therapy. In addition, a model-based algorithm has been developed to reconstruct quantitative dosimetry with XACT<sup>33</sup> (Fig. 2b). Furthermore, on a rabbit model, the therapeutic X-ray beam has been tracked in real time<sup>59</sup>. This achievement highlights the potential for precise beam localization during treatment.

The feasibility of using XACT for in vivo monitoring at multiple sites, including the prostate<sup>78</sup> and breast<sup>68,75</sup>, has also been demonstrated by computer simulations. These simulations show that XACT can accurately monitor high-dose regions within the prostate while sparing surrounding tissues, using trans-perineal ultrasound arrays<sup>32</sup>. This finding suggests that RAI could facilitate adaptive radiotherapy by producing real-time dose maps for each photon beam pulse, enabling dynamic adjustments to beam deliveries for optimal treatment efficacy (Fig. 2c).

A milestone achievement is the demonstration of the application of RAI in a patient with liver cancer in a clinical setting <sup>54</sup>. Qualitative dose reconstructions were overlaid on computed tomography scans of the patient, allowing clinicians to visualize and track dose deposition in real time, thereby ensuring that the treatment conformed to the planned protocol and enhancing control over dose delivery.

## Portable computed tomography

Beyond radiotherapy, RAI has been suggested as a portable alternative to traditional computed tomography scanners when using X-rays in the tens of kiloelectronvolts range<sup>8,10,67,68,79-81</sup>. XACT leverages

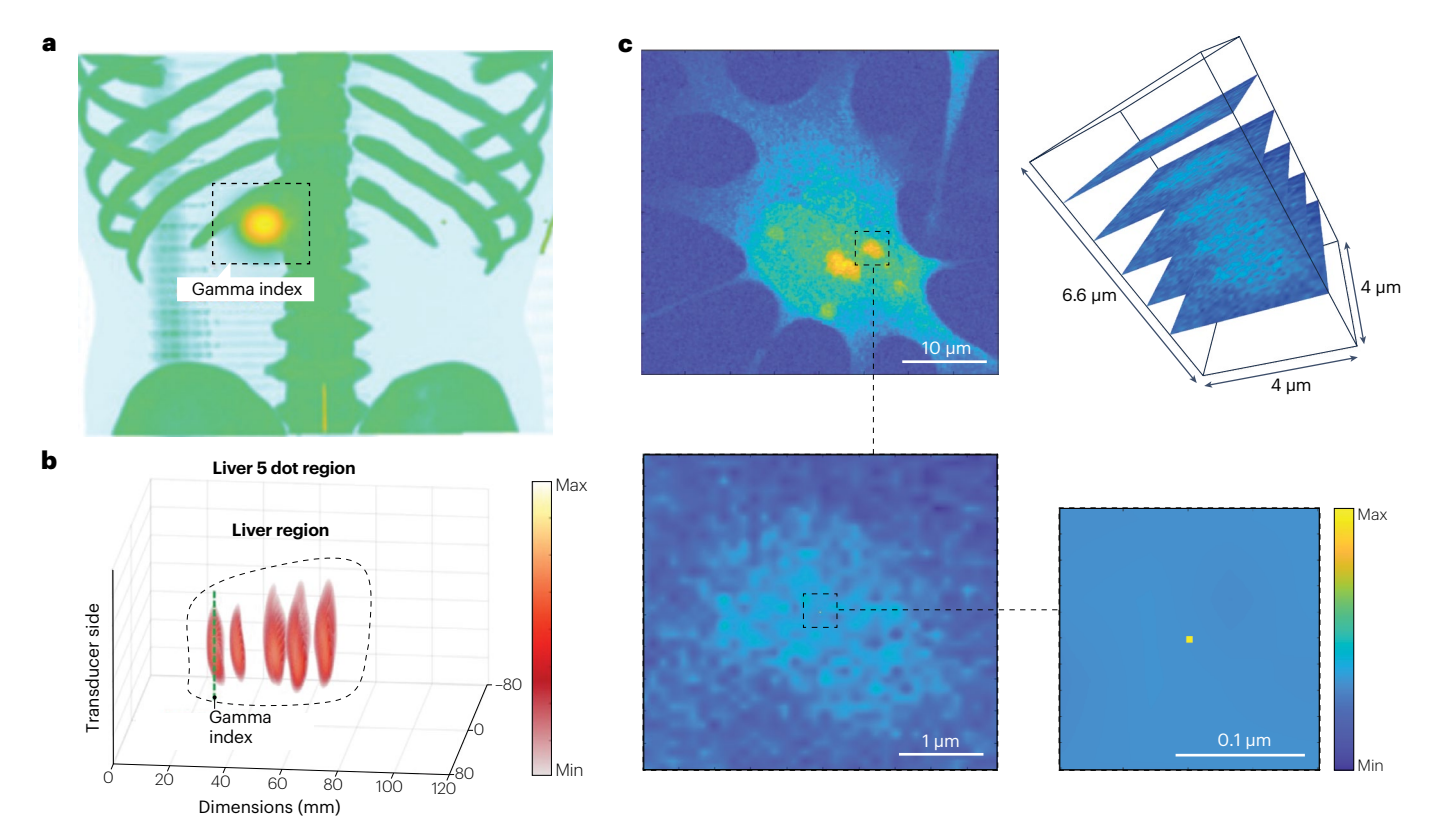


**Fig. 3** | **Radiacoustic imaging (RAI) using proton beams. a**, RAI of a dose to the liver (indicated by the box) overlaid with computed tomography image of the torso. **b**, 3D RAI of the Bragg peak at five different proton energies.

**c**, Computer simulations of single-cell imaging from proton-induced acoustic signals. Parts **a** and **b** adapted from ref. 16, CC BY 4.0. Part **c** adapted with permission from ref. 14, AIP.

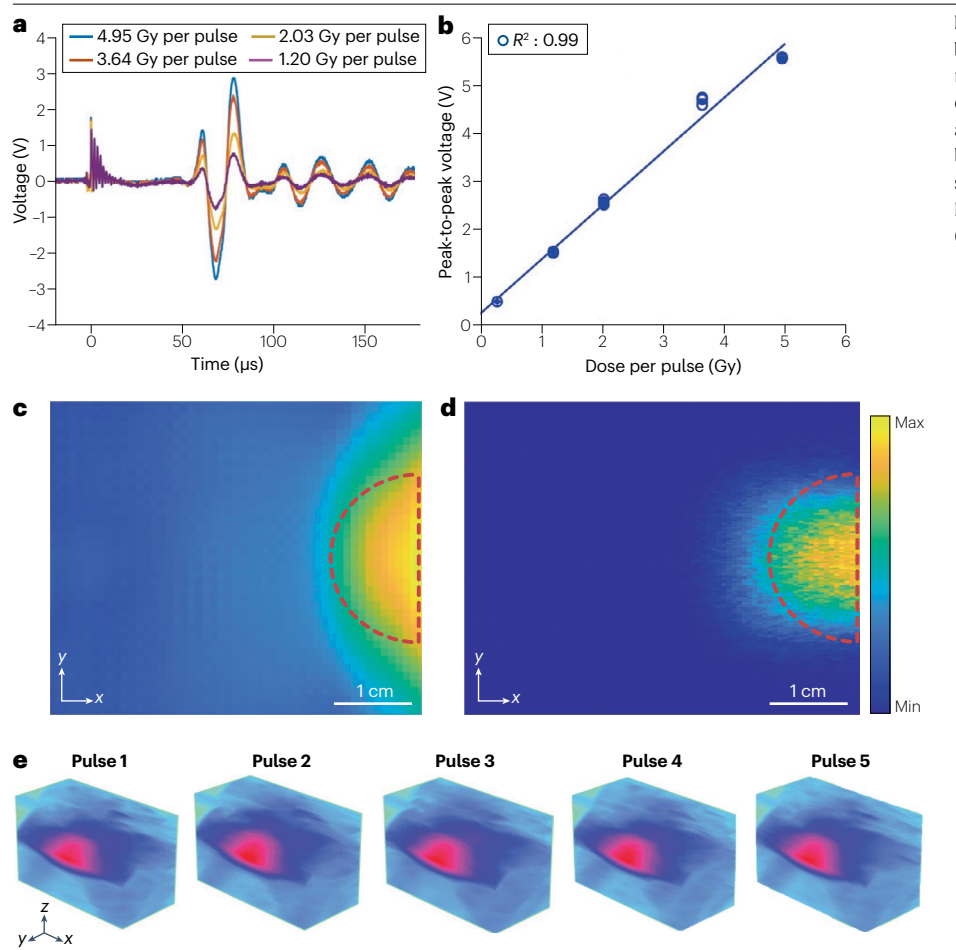


**Fig. 4** | **Radiacoustic imaging (RAI) using electron beams. a**, Radiacoustic signals obtained from FLASH radiation doses up to 4.95 Gy per pulse. **b**, Linearity of the relationship between measured peak-to-peak amplitude and applied dose. **c**,**d**, RAI of an electron beam (part **c**) and comparison with a Monte Carlo simulation (part **d**). **e**, 3D volumetric imaging of a FLASH electron beam in water taken at intervals of 0.1 s. Figure adapted with permission from ref. 18, IOP.

radiation-induced acoustic waves for 3D imaging from a single X-ray projection. This method has been validated through 3D numerical reconstructions and experimental determinations of bone structures at various depths (Fig. 2d), achieving high-resolution images and eliminating the need for mechanical scanning. It also shows the potential for molecular imaging when contrast agent is used 82. The potential of XACT extends to both biomedical applications and non-destructive testing, suggesting that it could eventually replace traditional computed tomography scanners in certain scenarios.

### RAI via proton excitation

Imaging techniques based on acoustic waves generated by proton beams are known as protoacoustic imaging <sup>15,55,83</sup>, thermoacoustic imaging <sup>17,48,60,62,84,85</sup> or ionoacoustic measurement <sup>61,86–88</sup>. Such techniques have been used in clinical settings to localize the Bragg peak during proton therapy (Fig. 3a) and have also shown potential for microscopic imaging using low-energy protons <sup>14</sup>.

#### Localizing the Bragg peak in proton therapy

High-energy protons (70–250 MeV) are used in radiotherapy to deliver precise treatments by taking advantage of the Bragg peak  $^{89-91}$ . The Bragg peak phenomenon ensures that most of the radiation is concentrated at a specific depth within the tissue, but this results in proton therapy presenting unique challenges in accurately monitoring dose

deposition 92,93. Unlike photon beams, proton beams do not traverse the entire patient, preventing the use of transmission proton imaging to track dose deposition 94,95. Traditional pretreatment simulations, which do not account for changes such as respiratory movement, often lead to inaccuracies 88,96,97. Moreover, routine clinical practice does not generally include replanning for changes such as tumour shrinkage, and thus real-time monitoring is needed 90,98,99. RAI offers compact, cost-effective systems that integrate easily into clinical workflows, enabling simultaneous dose monitoring and Bragg peak localization (Fig. 3b) without disrupting existing procedures.

Advances in RAI technology include the development of a 3D imaging system that uses a  $16 \times 16$  element 2D matrix array, which enhances the 3D localization of the Bragg peak during therapy  $^{16,32,65}$ . This system integrates ultrasonic transducers, multichannel pre-amplifiers and extensive data acquisition capabilities, allowing high-speed real-time imaging that is ideal for clinical environments and adaptive radiotherapy. Moreover, there is evidence for the effectiveness of RAI in tracking the Bragg peak during ultrahigh-dose-rate (known as FLASH) proton irradiations, suggesting that RAI offers a method for volumetric beam imaging at both conventional and FLASH dose rates  $^{65}$ .

## Microscopic imaging for single cells

When using low-energy protons (several MeV), proton-induced acoustic microscopy has been proposed as an advanced technique that

overcomes the resolution constraints of traditional optical microscopy, which is limited to approximately 200 nm owing to optical diffraction his advanced approach uses pulsed proton irradiation to generate and then collect proton-induced acoustic signals, providing label-free, super-resolution, 3D imaging from a single raster. A feasibility study involving Monte Carlo and k-wave simulations, based on a proton scanning transmission ion microscopy image of HeLa cells (Fig. 3c), shows that this technique can achieve sub-50-nm lateral and sub-micrometre axial resolutions  $^{14}$ . By enabling detailed visualization of cellular and subcellular structures, proton-induced acoustic microscopy may help with understanding cellular processes.

### RAI via electron excitation

Electron beams are also used in radiotherapy, offering effective treatment options particularly for superficial tumours due to their limited penetration depth compared with X-rays and protons¹00. An advanced application of electron beams is FLASH radiotherapy (FLASH-RT), which uses ultrahigh dose rates (≥100 Gy s⁻¹) and has shown lower toxicity in healthy tissues compared with conventional radiotherapy while effectively controlling tumours¹01. Preclinical studies across various tumour types have highlighted the potential of FLASH-RT to enhance the quality of life of patients by minimizing side effects without compromising therapeutic efficacy¹02. One notable clinical case involved treating a 75-year-old male patient who presented with CD30+ T cell cutaneous lymphoma using electron FLASH, where he received 15 Gy in 10 pulses without risk to organs or concerns about patient movement¹03.

Although FLASH-RT has shown promising results, broader clinical adoption may benefit from technologies that can offer real-time in vivo dosimetry. RAI shows promise as a reliable and effective tool for monitoring FLASH therapy at high dose rates<sup>18</sup>. RAI is primarily used to monitor FLASH therapies delivered via the most accessible electron beam lines. Simulations<sup>52</sup> and studies indicate that electron FLASH monitored with RAI achieves increased signal-to-noise ratios compared with conventional dose rates, owing to the high dose per pulse<sup>19</sup>, with dose-rate independence demonstrated across a range from 25 cGv to 5 Gy and dose rates up to  $2.75 \times 10^6$  Gy s<sup>-1</sup> (ref. 18). Notably, RAI does not show saturation even at doses as high as 4.95 Gy per pulse (Fig. 4a). Its linearity (Fig. 4b) compares favourably with traditional film measurements; however, film measurements do not offer in vivo dosimetry or provide a 3D dose distribution. Furthermore, the dose mapping with RAI (Fig. 4c) aligns closely with Monte Carlo simulations (Fig. 4d). A particular benefit of RAI is that it enables the real-time monitoring of each individual electron pulse, providing valuable 3D data (Fig. 4e). RAI monitoring in clinical settings is particularly advantageous for tumours located near radiosensitive tissues on extremities.

## RAI via pulsed electrical field

RAI can also be generated using non-ionizing methods, such as pulsed electrical fields<sup>28,38</sup>. The use of electrical therapy has advanced considerably since the eighteenth century when electric fields were noted to cause tissue damage<sup>27,104</sup>. Subsequent research led to the development of electroporation, a method that uses pulsed electric fields to enhance the permeability of cell membranes, aiding the uptake of substances such as drugs or DNA<sup>105,106</sup>. This technique has found application across fields including DNA transfection<sup>107</sup>, electrochemotherapy<sup>108</sup> and tissue ablation<sup>109</sup>, with its effectiveness influenced by the specific parameters of the electrical pulses. However, despite its widespread

use, real-time monitoring of electroporation effects in deep tissues remains challenging because of the limitations of existing imaging technologies<sup>27</sup>.

Electroacoustic tomography addresses this challenge by detecting the ultrasound waves generated by pulsed electrical fields<sup>27,28,69,70</sup>. In one electroacoustic tomography imaging system, nanosecond electrical pulses were provided from a high-voltage pulse generator coupled with a tungsten electrode set to generate detectable electroacoustic signals<sup>27</sup>. These pulses, nearly square with a 100-ns FWHM and a repetition rate of up to 1 MHz, are captured by an ultrasonic transducer, then amplified and digitized for analysis. Experiments use a 128-element, 5-MHz ring ultrasound array processed by a 128-channel data

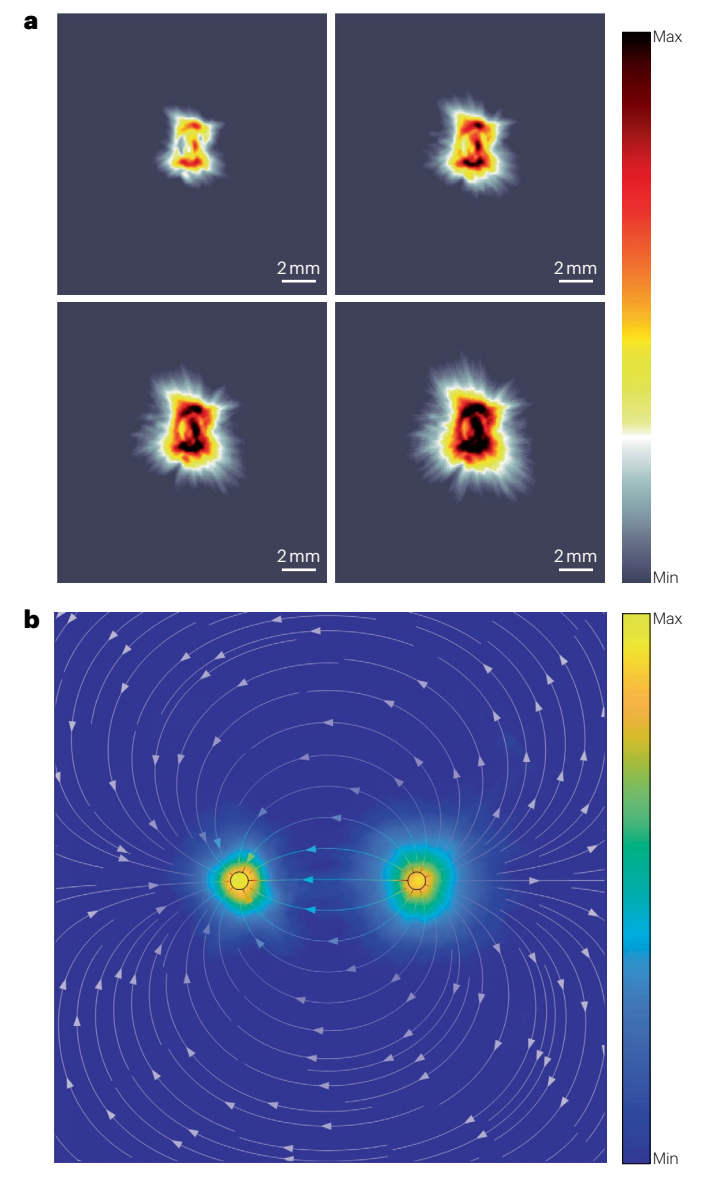


**Fig. 5** | **Radiacoustic imaging (RAI) via pulsed electrical field. a**, RAI maps of electrical field energy distribution in a chicken breast sample, taken sequentially at intervals of 375 ms (a rate of 75 frames per second). **b**, RAI visualization of the electric field between two electrodes in a 1% saline solution. Part **a** adapted from ref. 27, CC BY 4.0. Part **b** adapted with permission from ref. 110, AIP.

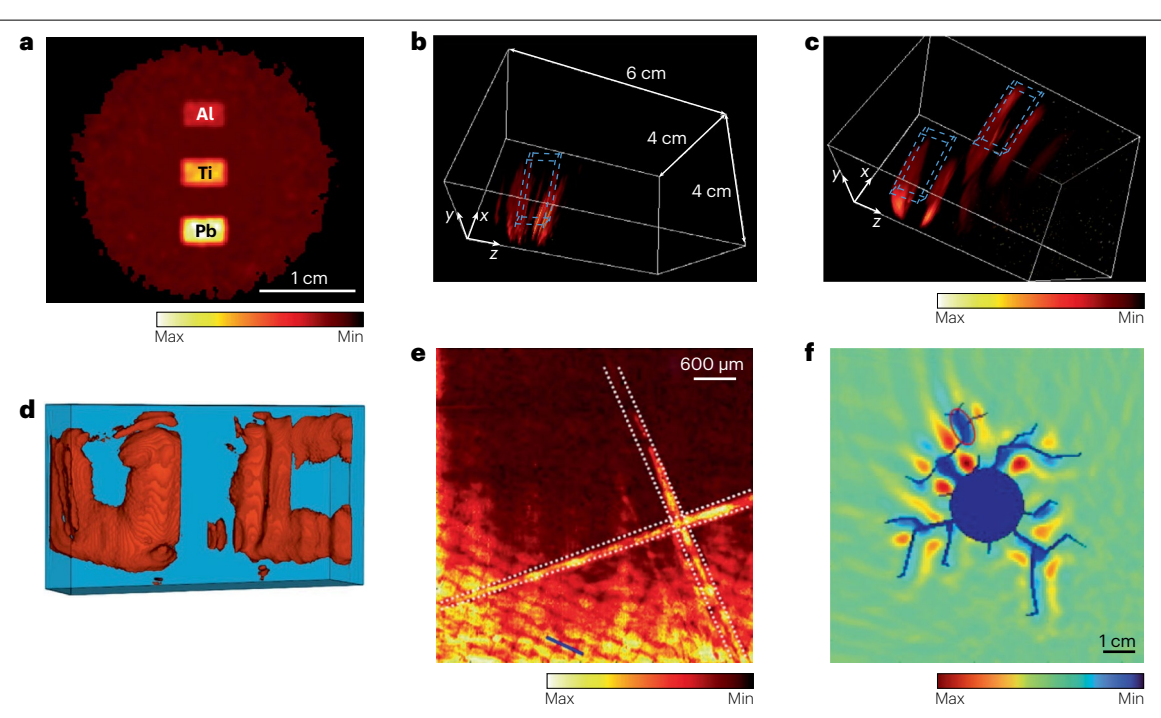


**Fig. 6 | Radiacoustic imaging (RAI) and its application in material science. a**, Protoacoustic radiography provides contrast among various materials (AI, Ti, Pb). **b**, **c**, 3D RAI images acquired at selected proton energies for different depths. **d**, RAI obtains 3D images from a single X-ray projection of the UC logo. **e**, Imaging of cracks around rebar in concrete, using X-ray-induced acoustic

computed tomography. **f**, Detection of damage in carbon-fibre-reinforced polymer composites via laser excitation. Parts **a**–**c** adapted with permission from ref. 111, AIP. Part **d** adapted with permission from ref. 10, AAAS. Part **e** adapted from ref. 116, CC BY 4.0. Part **f** adapted with permission from ref. 115, AIP.

acquisition system that enables high-resolution, real-time visualization of electric field dynamics within tissues using a filtered back-projection algorithm. Electroacoustic tomography can be used to monitor the energy deposition during electroporation in real time at submillimetre resolution up to 7.5 cm deep and at imaging speeds of 75 frames per second (Fig. 5a). It detects signals across a wide range of electric field strengths, from 60 V cm<sup>-1</sup> to several tens of kilovolts per centimetre, making it a high-resolution, label-free method for evaluating deep tissue electroporation during therapy.

Recently, instead of capturing electroacoustic signals using PZT (lead zirconate titanate) transducers, an optical interferometer-based system has been developed  $^{110}$ . This system can detect electroacoustic signals in a non-contact manner. A 24-channel detector array captures the interference signals. A multimode fibre transmits the incident laser beam to the optical head and collects the backscattered object beam. The output signal is then amplified by 60 dB and recorded on an oscilloscope. Figure 5b shows the electrical energy distribution. Additionally, the non-contact electroacoustic signal acquisition capability of this interferometer-based system eliminates the need for physical contact via coupling media and is not sensitive to electromagnetic interference, thereby enhancing the clinical translation capability.

## RAI and its applications in materials science

RAI is expanding its reach beyond biomedical applications, with potential applications in materials science and non-destructive evaluation (NDE)<sup>10,111</sup>. Traditional NDE techniques – such as acoustic emission, infrared thermography and ultrasonic testing – are widely used, but each has limitations. For example, acoustic emission is

effective for in situ damage characterization by monitoring elastic waves released from structural defects, but it may not detect initial damage stages<sup>112</sup>. Infrared thermography can identify subsurface defects such as cracking and delamination in composites, but it often fails to locate damage precisely through the material thickness<sup>113</sup>. Ultrasonic methods, including Lamb wave and tomographic imaging, can detect various damage types in composites but struggle with microscale damage detection<sup>114</sup>.

RAI techniques show promise in various situations. Protoacoustic radiography<sup>111</sup>, besides being depth selective, overcomes issues such as multiple Coulomb scattering and can distinguish different materials (Al, Ti, Pb) (Fig. 6a), correlating well with simulations. Protoacoustic radiography has successfully reconstructed targets at various depths, demonstrating its utility in NDE (Fig. 6b,c). RAI via X-ray excitation<sup>10</sup> enables 3D imaging of objects from a single projection (Fig. 6d). It also shows potential for imaging rebar and detecting surrounding defects in concrete materials<sup>115</sup> (Fig. 6e). Systems that use laser-induced ultrasonics generate high-frequency ultrasonic signals that effectively detect damage in materials such as carbon-fibre-reinforced polymer composites<sup>116</sup> (Fig. 6f). The choice of radiation source in material science largely depends on the specific application. For colour-coded materials with varying optical absorption wavelengths, laser excitation is a good option, although limited by shallow penetration. For deeper imaging, X-rays or protons are more suitable.

#### **Outlook**

The development of RAI may offer several benefits. RAI detects signals from radiation dose deposition within a patient<sup>18,33,54,65,77,117</sup>. This

is particularly valuable for deep-seated tumours, where alternative in vivo dosimetry methods are limited. Moreover, a key clinical need today is a real-time dosimetric readout that works reliably across both conventional and FLASH radiotherapy. Such a solution does not yet exist, but RAI has demonstrated promise in meeting this need, thanks to its large dynamic range and compatibility with both modalities. Furthermore, RAI uses ultrasound detectors positioned outside the path of the radiation beam, avoiding interference with treatment delivery. The system is portable, easily adaptable to clinical environments and particularly well suited for imaging organs commonly assessed by ultrasound, such as the breast 66,75, prostate 32,71 and liver 54.

Although the first patient study has already been completed<sup>54</sup>, broader clinical adoption requires further validation and regulatory approval. Whereas mapping the path of the radiation beam is relatively straightforward, accurate dose quantification is more complex. Radiacoustic signal strength does correlate with dose deposition, but challenges such as acoustic attenuation, sound speed heterogeneity and limited-view reconstruction must be overcome. Fortunately, model-based reconstruction and deep learning approaches are emerging that may address these limitations<sup>7,10</sup>.

Beyond radiotherapy, RAI offers a fundamentally new imaging paradigm: converting X-ray or proton energy deposition into spherical ultrasound waves, which enables 3D imaging from a single projection. This capability is unattainable with conventional X-ray computed tomography<sup>10</sup> or proton radiography<sup>111</sup>. It provides real-time imaging capability and the potential for gantry-free computed tomography systems that greatly change imaging workflows. This feature expands the potential applications of RAI well beyond biomedicine to include material characterization and industrial non-destructive testing.

Moreover, RAI allows for the visualization of otherwise invisible energy fields<sup>27,110</sup>, such as electric fields generated during irreversible electroporation or ablation therapies for atrial fibrillation. When integrated with pulse–echo ultrasound through the same transducers, RAI can provide real-time guidance for dynamic processes such as tumour motion tracking during therapy or needle placement during interventional procedures<sup>59</sup>.

Despite its potential, RAI faces several technical challenges, four of which we outline here. First, enhancing detector sensitivity is critical for detecting weak signals from deep tissues. Dual-frequency or broadband transducers may be required to detect both low-frequency radiacoustic signals and high-frequency pulse–echo ultrasound. Purpose-built detectors that meet the specific bandwidth and sensitivity needs of RAI will outperform conventional ultrasound transducers adapted for this role<sup>118</sup>.

Second, although back-projection methods are commonly used for image reconstruction owing to their simplicity, they are limited by assumptions of homogeneity and complete angular coverage. To address these challenges, advanced model-based reconstruction methods have been developed <sup>49,50</sup>. These approaches explicitly incorporate the physics of acoustic wave propagation and account for heterogeneous tissue properties – such as spatial variations in the speed of sound, density and acoustic attenuation – within both the forward and inverse modelling processes. By doing so, they offer improved accuracy over analytical methods such as universal back-projection, particularly in anatomically complex environments.

In parallel, machine-learning-based algorithms 11,51,64 are also being developed to overcome the limitations of traditional reconstruction techniques. These methods, often trained on paired datasets of

limited-view and full-view images (or high-quality simulations), learn to recover missing spatial information and suppress artefacts. This is especially useful in scenarios with limited detector coverage or strong acoustic heterogeneity.

Additionally, the spatial variation of the Grüneisen parameter in heterogeneous tissues can affect RAI image accuracy. This issue can be mitigated by incorporating prior anatomical information – such as planning computed tomography scans – which are commonly available in radiotherapy workflows. Together, these advances are paving the way toward more robust and clinically applicable RAI.

Third, diagnostic RAI will benefit from new high-repetition pulsed X-ray sources. Developments in laser-driven X-ray technologies — offering short pulses (nanoseconds or less), high repetition rates (>100 Hz) and broad energy ranges (keV to MeV) $^{119,120}$  — position them as ideal excitation sources for next-generation RAI systems.

Finally, radiation pulses delivered at ultrahigh dose rates in emerging FLASH radiotherapy (up to 42 Gy per pulse) can generate high-intensity, low-frequency thermoacoustic emissions that may induce cavitation and potentially have biological effects<sup>121</sup>. However, these predictions are based on simulation studies, and no experimental evidence has yet confirmed the presence of nonlinear acoustic effects under these conditions. With human studies having commenced in 2023<sup>54</sup>, there is an urgent need to define regulatory frameworks and standards for clinical use. This includes harmonizing system design, operational protocols and data analysis approaches.

Published online: 17 September 2025

#### References

- El Kaffas, A. et al. Quantitative three-dimensional dynamic contrast-enhanced ultrasound imaging: first-in-human pilot study in patients with liver metastases. *Theranostics* 7, 3745–3758 (2017).
- Sendra-Balcells, C. et al. Generalisability of fetal ultrasound deep learning models to low-resource imaging settings in five African countries. Sci. Rep. 13, 2728 (2023).
- Zhou, S. et al. Transcranial volumetric imaging using a conformal ultrasound patch. Nature 629, 810–818 (2024).
- Wang, F. et al. Flexible Doppler ultrasound device for the monitoring of blood flow velocity. Sci. Adv. 7, eabi9283 (2021).
- Wang, L. V. & Hu, S. Photoacoustic tomography: in vivo imaging from organelles to organs. Science 335, 1458–1462 (2012).
- Xiang, L., Tang, S., Ahmad, M. & Xing, L. High resolution X-ray-induced acoustic tomography. Sci. Rep. 6, 26118 (2016).
- Pandey, P. K. et al. Model-based X-ray-induced acoustic computed tomography. IEEE Trans. Ultrason. Ferroelectr. Freq. Control. 68, 3560–3569 (2021).
- Robertson, E. et al. X-ray-induced acoustic computed tomography (XACT): initial experiment on bone sample. IEEE Trans. Ultrason. Ferroelectr. Freq. Control. 68, 1073–1080 (2021).
- Yan, Y. & Xiang, S. L. X-ray-induced acoustic computed tomography and its applications in biomedicine. J. Biomed. Opt. 29, S11510 (2024).
- Wang, S. et al. X-ray-induced acoustic computed tomography: 3D X-ray absorption imaging from a single view. Sci. Adv. 10, eads1584 (2024).
- Jiang, Z. et al. 3D in vivo dose verification in prostate proton therapy with deep learning-based proton-acoustic imaging. Phys. Med. Biol. 67, 215012 (2022).
- Hayakawa, Y. et al. Acoustic pulse generated in a patient during treatment by pulsed proton radiation beam. Radiat. Oncol. Investig. 3, 42-45 (1995).
- Jones, K. C. et al. Experimental observation of acoustic emissions generated by a pulsed proton beam from a hospital-based clinical cyclotron. Med. Phys. 42, 7090–7097 (2015).
- Pandey, P. K. et al. Ionic-resolution protoacoustic microscopy: a feasibility study Appl. Phys. Lett. 124, 053702 (2024).
- Nie, W. et al. Proton range verification in homogeneous materials through acoustic measurements. Phys. Med. Biol. 63, 025036 (2018).
- Wang, S. et al. Real-time tracking of the Bragg peak during proton therapy via 3D protoacoustic imaging in a clinical scenario. NPJ Imaging 2, 34 (2024).
- Patch, S. K. et al. Thermoacoustic range verification during pencil beam delivery of a clinical plan to an abdominal imaging phantom. Radiother. Oncol. 159, 224-230 (2021).
- Bjegovic, K. et al. 4D in vivo dosimetry for a FLASH electron beam using radiation-induced acoustic imaging. Phys. Med. Biol. https://doi.org/10.1088/1361-6560/ ad4950 (2024).
- Oraiqat, I. et al. An ionizing radiation acoustic imaging (iRAI) technique for real-time dosimetric measurements for FLASH radiotherapy, Med. Phys. 47, 5090-5101 (2020).

- Gao, X. et al. A photoacoustic patch for three-dimensional imaging of hemoglobin and core temperature. Nat. Commun. 13, 7757 (2022).
- 21. Xiang, L., Wang, B., Ji, L. & Jiang, H. 4-D photoacoustic tomography. Sci. Rep. 3, 1113 (2013).
- Lao, Y., Xing, D., Yang, S. & Xiang, L. Noninvasive photoacoustic imaging of the developing vasculature during early tumor growth. *Phys. Med. Biol.* 53, 4203–4212 (2008).
- Xiang, L. et al. Photoacoustic molecular imaging with antibody-functionalized single-walled carbon nanotubes for early diagnosis of tumor. J. Biomed. Opt. 14, 021008 (2009).
- 24. Wang, B. et al. Photoacoustic tomography system for noninvasive real-time three-dimensional imaging of epilepsy. *Biomed. Opt. Express* **3**, 1427 (2012).
- Li, L., Li, Y., Zhang, Y. & Wang, L. V. Snapshot photoacoustic topography through an ergodic relay of optical absorption in vivo. Nat. Protoc. 16, 2381–2394 (2021).
- Lin, L. & Wang, L. V. The emerging role of photoacoustic imaging in clinical oncology. Nat. Rev. Clin. Oncol. 19, 365–384 (2022).
- Xu, Y. et al. Electroacoustic tomography for real-time visualization of electrical field dynamics in deep tissue during electroporation. Commun. Eng. 2, 75 (2023).
- Wang, S., Zarafshani, A. & Xiang, L. Electroacoustic tomography (EAT): 2D electric field reconstruction for electroporation treatment monitoring. SPIE Med. Imaging 2021 11598, 1159820 (2021).
- Roth, C. C. et al. Characterization of pressure transients generated by nanosecond electrical pulse (nsEP) exposure. Sci. Rep. 5, 15063 (2015).
- Kumar Pandey, P. et al. Resolution limits for radiation-induced acoustic imaging for in vivo radiation dosimetry. Phys. Med. Biol. https://doi.org/10.1088/1361-6560/ad64b9 (2024)
- 31. Beard, P. Biomedical photoacoustic imaging. Interface Focus 1, 602-631 (2011).
- Wang, M. et al. Toward in vivo dosimetry for prostate radiotherapy with a transperineal ultrasound array: a simulation study. IEEE Trans. Radiat. Plasma Med. Sci. 5, 373–382 (2021).
- Sun, L. et al. Towards quantitative in vivo dosimetry using Xray acoustic computed tomography. Med. Phys. https://doi.org/10.1002/mp.16476 (2023).
- Wang, L. V. & Yao, J. A practical guide to photoacoustic tomography in the life sciences. Nat. Methods 13, 627–638 (2016).
- Park, J. et al. Clinical translation of photoacoustic imaging. Nat. Rev. Bioeng. 3, 193–212 (2025)
- Kim, C., Favazza, C. & Wang, L. V. In vivo photoacoustic tomography of chemicals: high-resolution functional and molecular optical imaging at new depths. Chem. Rev. 110, 2756–2782 (2010).
- Xu, M. & Wang, L. V. Photoacoustic imaging in biomedicine. Rev. Sci. Instrum. 77, 041101 (2006).
- Li, C. & Wang, L. V. Photoacoustic tomography and sensing in biomedicine. Phys. Med. Biol. 54, R59 (2009).
- 39. Wang, L. V. Prospects of photoacoustic tomography. Med. Phys. 35, 5758-5767 (2008).
- Ntziachristos, V. & Razansky, D. Molecular imaging by means of multispectral optoacoustic tomography (MSOT). Chem. Rev. 110, 2783–2794 (2010).
- Zhang, H. F., Maslov, K., Stoica, G. & Wang, L. V. Functional photoacoustic microscopy for high-resolution and noninvasive in vivo imaging. Nat. Biotechnol. 24, 848–851 (2006).
- Wang, X. et al. Noninvasive laser-induced photoacoustic tomography for structural and functional in vivo imaging of the brain. Nat. Biotechnol. 21, 803–806 (2003).
- Maslov, K., Zhang, H. F., Hu, S. & Wang, L. V. Optical-resolution photoacoustic microscopy for in vivo imaging of single capillaries. Opt. Lett. 33, 929–931 (2008).
- Razansky, D. et al. Multispectral opto-acoustic tomography of deep-seated fluorescent proteins in vivo. Nat. Photon. 3, 412–417 (2009).
- Xu, M. & Wang, L. V. Universal back-projection algorithm for photoacoustic computed tomography. *Phys. Rev. E* 71, 016706 (2005).
- Samant, P., Trevisi, L. M., Chen, Y., Zwart, T. & Xiang, L. 3-D protoacoustic imaging through a planar ultrasound array: a simulation workflow. *IEEE Trans. Radiat. Plasma Med. Sci.* 7, 83–95 (2023).
- Treeby, B. E., Zhang, E. Z. & Cox, B. T. Photoacoustic tomography in absorbing acoustic media using time reversal. *Inverse Probl.* 26, 115003 (2010).
- Mast, T. D., Johnstone, D. A., Dumoulin, C. L., Lamba, M. A. & Patch, S. K. Reconstruction of thermoacoustic emission sources induced by proton irradiation using numerical time reversal. *Phys. Med. Biol.* https://doi.org/10.1088/1361-6560/acabfc (2023).
- Razansky, D. & Deán-Ben, X. L. A practical guide for model-based reconstruction in optoacoustic imaging. Front. Phys. https://doi.org/10.3389/fphy.2022.1028258 (2022).
- Pandey, P. K., Wang, S., Sun, L., Xing, L. & Xiang, L. Model-based 3-D X-ray induced acoustic computerized tomography. *IEEE Trans. Radiat. Plasma Med. Sci.* 7, 532–543 (2023).
- Lang, Y., Jiang, Z., Sun, L., Xiang, L. & Ren, L. Hybrid-supervised deep learning for domain transfer 3D protoacoustic image reconstruction. https://doi.org/10.48550/ ARXIV.2308.06194 (2023).
- Ba Sunbul, N. et al. A simulation study of ionizing radiation acoustic imaging (iRAI) as a real-time dosimetric technique for ultra high dose rate radiotherapy (UHDR-RT). Med. Phys. 48, 6137–6151 (2021).
- Xiang, L. et al. X-ray acoustic computed tomography with pulsed X-ray beam from a medical linear accelerator. Med. Phys. 40, 010701 (2012).
- Zhang, W. et al. Real-time, volumetric imaging of radiation dose delivery deep into the liver during cancer treatment. *Nat. Biotechnol.* https://doi.org/10.1038/s41587-022-01593-8 (2023)
- Caron, J. et al. Single pulse protoacoustic range verification using a clinical synchrocyclotron. Phys. Med. Biol. 68, 045011 (2023).

- Lehrack, S. et al. Submillimeter ionoacoustic range determination for protons in water at a clinical synchrocyclotron. Phys. Med. Biol. 62, L20–L30 (2017).
- Hickling, S. et al. Experimental evaluation of X-ray acoustic computed tomography for radiotherapy dosimetry applications. Med. Phys. 44, 608–617 (2017).
- 58. Gonzalez, G. et al. Single-pulse X-ray acoustic computed tomographic imaging for precision radiation therapy. *Adv. Radiat. Oncol.* **8**, 101239 (2023).
- Zhang, W. et al. Dual-modality X-ray-induced radiation acoustic and ultrasound imaging for real-time monitoring of radiotherapy. BME Front. 2020, 9853609 (2020).
- Patch, S. K. et al. Thermoacoustic range verification using a clinical ultrasound array provides perfectly co-registered overlay of the Bragg peak onto an ultrasound image. *Phys. Med. Biol.* 61, 5621–5638 (2016).
- Schauer, J. et al. Range verification of a clinical proton beam in an abdominal phantom by co-registration of ionoacoustics and ultrasound. Phys. Med. Biol. 68, 125009 (2023).
- Lascaud, J. et al. Investigating the accuracy of co-registered ionoacoustic and ultrasound images in pulsed proton beams. Phys. Med. Biol. https://doi.org/10.1088/1361-6560/ac215e (2021).
- Tang, S. et al. X-ray-induced acoustic computed tomography with an ultrasound transducer ring-array. Appl. Phys. Lett. 110, 103504 (2017).
- Pandey, P. K. et al. Ring artifacts removal in X-ray-induced acoustic computed tomography. J. Innov. Opt. Health Sci. 15, 2250017 (2022).
- Wang, S. et al. Toward real-time, volumetric dosimetry for FLASH-capable clinical synchrocyclotrons using protoacoustic imaging. Med. Phys. https://doi.org/10.1002/ mp.17318 (2024).
- Shen, L., Zhao, W. & Xing, L. Patient-specific reconstruction of volumetric computed tomography images from a single projection view via deep learning. Nat. Biomed. Eng. 3, 880–888 (2019).
- Li, Y. et al. 3-D X-ray-induced acoustic computed tomography with a spherical array: a simulation study on bone imaging. *IEEE Trans. Ultrason. Ferroelectr. Freq. Control.* 67, 1613–1619 (2020).
- Tang, S., Yang, K., Chen, Y. & Xiang, L. X-ray-induced acoustic computed tomography for 3D breast imaging: a simulation study. *Med. Phys.* 45, 1662–1672 (2018).
- Jiang, Z. et al. Radiation-induced acoustic signal denoising using a supervised deep learning framework for imaging and therapy monitoring. *Phys. Med. Biol.* https://doi.org/ 10.1088/1361-6560/ad0283 (2023).
- Jiang, Z. et al. Enhanced electroacoustic tomography with supervised learning for real-time electroporation monitoring. Precis. Radiat. Oncol. 8, 110–118 (2024).
- Lang, Y. et al. Patient-specific deep learning for 3D protoacoustic image reconstruction and dose verification in proton therapy. Med. Phys. 51, 7425–7438 (2024).
- Yao, J. & Wang, L. V. Photoacoustic microscopy. Laser Photonics Rev. https://doi.org/10.1002/ lpor.201200060 (2013).
- Xing, L. et al. Overview of image-guided radiation therapy. Med. Dosimetry 31, 91–112 (2006).
- Dong, P. et al. 4π non-coplanar liver SBRT: a novel delivery technique. Int. J. Radiat. Oncol. Biol. Phys. 85, 1360–1366 (2013).
- Zheng, Y. et al. X-ray-induced acoustic computed tomography for guiding prone stereotactic partial breast irradiation: a simulation study. Med. Phys. 47, 4386–4395 (2020).
- Sampaio, D. R. T. et al. X-ray acoustic imaging for external beam radiation therapy dosimetry using a commercial ultrasound scanner. In 2015 IEEE International Ultrasonics Symposium (IUS) https://doi.org/10.1109/ULTSYM.2015.0400 (IEEE, 2015).
- Lei, H. et al. Toward in vivo dosimetry in external beam radiotherapy using X-ray acoustic computed tomography: a soft-tissue phantom study validation. Med. Phys. 45, 4191–4200 (2018).
- Hickling, S., Hobson, M. & El Naqa, I. Feasibility of X-ray acoustic computed tomography as a tool for noninvasive volumetric in vivo dosimetry. *Int. J. Radiat. Oncol.\*Biol.\*Phys.* 90, S843 (2014).
- Wang, S., Ivanov, V., Pandey, P. K. & Xiang, L. X-ray-induced acoustic computed tomography (XACT) imaging with single-shot nanosecond X-ray. Appl. Phys. Lett. 119, 183702 (2021).
- Choi, S. et al. X-ray free-electron laser induced acoustic microscopy (XFELAM) Photoacoustics 35, 100587 (2024).
- Choi, S., Park, E.-Y., Park, S., Kim, J. H. & Kim, C. Synchrotron X-ray induced acoustic imaging. Sci. Rep. 11, 4047 (2021).
- Lee, D. et al. GPU-accelerated 3D volumetric X-ray-induced acoustic computed tomography. Biomed. Opt. Express 11, 752-761 (2020).
- Jones, K. C. et al. Acoustic-based proton range verification in heterogeneous tissue: simulation studies. Phys. Med. Biol. 63, 025018 (2018).
- Patch, S. K., Santiago-Gonzalez, D. & Mustapha, B. Thermoacoustic range verification in the presence of acoustic heterogeneity and soundspeed errors — robustness relative to ultrasound image of underlying anatomy. *Med. Phys.* 46, 318–327 (2019).
- Lascaud, J., Rädler, M., Rohrer Bley, C., Vozenin, M.-C. & Parodi, K. Retrospective study on the resonance of thermoacoustic emissions and their possible biological implications in cats treated with electron FLASH beams. *Phys. Med. Biol.* 70, 055013 (2025).
- Kirsch, L. et al. Ionoacoustic monitoring of relativistic heavy ion beams. Nucl. Instrum. Methods A 1057, 168755 (2023).
- Kalunga, R. et al. On the robustness of multilateration of ionoacoustic signals for localization of the Bragg peak at pre-clinical proton beam energies in water. *Phys. Med. Biol.* 68, 105010 (2023).
- Schauer, J. et al. Proton beam range verification by means of ionoacoustic measurements at clinically relevant doses using a correlation-based evaluation. Front. Oncol. 12, 925542 (2022).

- Durante, M. Proton beam therapy in Europe: more centres need more research. Br. J. Cancel 120, 777-778 (2019).
- Mohan, R. A review of proton therapy current status and future directions. Precis. Radiat. Oncol. 6. 164–176 (2022).
- Olsen, D. R., Bruland, Ø. S., Frykholm, G. & Norderhaug, I. N. Proton therapy a systematic review of clinical effectiveness. *Radiother. Oncol.* 83, 123–132 (2007).
- Lane, S. A., Slater, J. M. & Yang, G. Y. Image-guided proton therapy: a comprehensive review. Cancers 15, 2555 (2023).
- Knopf, A.-C. & Lomax, A. In vivo proton range verification: a review. Phys. Med. Biol. 58, R131–R160 (2013).
- Paganetti, H. Range uncertainties in proton therapy and the role of Monte Carlo simulations. Phys. Med. Biol. 57, R99–R117 (2012).
- 95. Lomax, A. J. Myths and realities of range uncertainty. Br. J. Radiol. 93, 20190582 (2020).
- O'Shea, T. et al. Review of ultrasound image guidance in external beam radiotherapy part II: intra-fraction motion management and novel applications. *Phys. Med. Biol.* 61, R90 (2016).
- Parodi, K. Latest developments in in-vivo imaging for proton therapy. Br. J. Radiol. 93, 20190787 (2020).
- Parodi, K. & Assmann, W. Ionoacoustics: a new direct method for range verification. Mod. Phys. Lett. A 30, 1540025 (2015).
- Parodi, K. & Polf, J. C. In vivo range verification in particle therapy. Med. Phys. 45, e1036–e1050 (2018).
- Renard, S., Parent, L., de Marzi, L., Tsoutsou, P. & Kirova, Y. Electron radiation therapy: back to the future? Cancer Radiother. 28, 553–559 (2024).
- Schüler, E. et al. Ultra-high dose rate electron beams and the FLASH effect: from preclinical evidence to a new radiotherapy paradigm. Med. Phys. 49, 2082–2095 (2022).
- McGarrigle, J. M., Long, K. R. & Prezado, Y. The FLASH effect an evaluation of preclinical studies of ultra-high dose rate radiotherapy. Front. Oncol. 14, 1340190 (2024).
- Bourhis, J. et al. Treatment of a first patient with FLASH-radiotherapy. Radiother. Oncol. 139, 18–22 (2019).
- Deipolyi, A. R., Golberg, A., Yarmush, M. L., Arellano, R. S. & Oklu, R. Irreversible electroporation: evolution of a laboratory technique in interventional oncology. *Diagn. Interv. Radiol.* 20, 147–154 (2014).
- Chu, G., Hayakawa, H. & Berg, P. Electroporation for the efficient transfection of mammalian cells with DNA. Nucleic Acids Res. 15, 1311–1326 (1987).
- Belehradek, M. et al. Electrochemotherapy, a new antitumor treatment. First clinical phase I-II trial. Cancer 72, 3694–3700 (1993).
- Potter, H. & Heller, R. Transfection by electroporation. Curr. Protoc. Mol. Biol. https://doi.org/10.1002/0471142727.mb0903s92 (2003).
- Hadzialjevic, B. et al. Electrochemotherapy combined with immunotherapy a promising potential in the treatment of cancer. Front. Immunol. 14, 1336866 (2024).
- Rubinsky, B., Onik, G. & Mikus, P. Irreversible electroporation: a new ablation modality — clinical implications. Technol. Cancer Res. Treat. 6, 37-48 (2007).
- Xu, Y., Song, Y., Sun, L., Chen, Z. & Xiang, L. Non-contact electroacoustic tomography with optical interferometer for electroporation therapy monitoring. *Appl. Phys. Lett.* 126, 023704 (2025).
- Pandey, P. K. et al. 3D protoacoustic radiography: a proof of principle study. Appl. Phys. Lett. 126, 074102 (2025).
- Noh, S. Z. et al. Advancements in acoustic emissions for civil structural engineering monitoring: a research and application review. Int. J. Eng. Trends Technol. 72, 234–246 (2024)

- Steinberger, R. et al. Infrared thermographic techniques for non-destructive damage characterization of carbon fibre reinforced polymers during tensile fatigue testing. *Int. J. Fatigue* 28, 1340–1347 (2006).
- Chang, Q., Peng, T. & Liu, Y. Tomographic damage imaging based on inverse acoustic wave propagation using k-space method with adjoint method. *Mech. Syst. Signal. Process.* 109, 379–398 (2018).
- Tang, S. S., Ramseyer, C., Samant, P. & Xiang, L. Z. X-ray-induced acoustic computed tomography of concrete infrastructure. *Appl. Phys. Lett.* 112, 063504 (2018).
- Wang, S. et al. Ultrahigh resolution pulsed laser-induced photoacoustic detection of multi-scale damage in CFRP composites. Appl. Sci. 10, 2106 (2020).
- 117. Kim, K., Pandey, P. K., Gonzalez, G., Chen, Y. & Xiang, L. Simulation study of protoacoustics as a real-time in-line dosimetry tool for FLASH proton therapy. *Med. Phys.* https://doi.org/ 10.1002/mp.16894 (2023).
- Vallet, M. et al. Quantitative comparison of PZT and CMUT probes for photoacoustic imaging: experimental validation. *Photoacoustics* 8, 48–58 (2017).
- Hannasch, A. et al. Compact spectroscopy of keV to MeV X-rays from a laser wakefield accelerator. Sci. Rep. 11, 14368 (2021).
- Ostermayr, T. M. et al. Laser-driven X-ray and proton micro-source and application to simultaneous single-shot bi-modal radiographic imaging. Nat. Commun. 11, 6174 (2020).
- Lascaud, J. & Parodi, K. On the potential biological impact of radiation-induced acoustic emissions during ultra-high dose rate electron radiotherapy: a preliminary study. Phys. Med. Biol. 68, 05LTOI (2023).

#### **Acknowledgements**

This work was supported by the National Institute of Health (R37CA240806, U01CA288351 and R50CA283816). The authors acknowledge support from UCI Chao Family Comprehensive Cancer Center (P30CA062203).

#### **Author contributions**

Y.X. contributed to figure preparation, literature citation and portions of the manuscript writing. S.X. conceived the overall structure of the manuscript and contributed to its writing.

#### **Competing interests**

The authors declare no competing interests.

#### Additional information

**Peer review information** *Nature Reviews Physics* thanks Julie Lascaud, Lihong Wang and the other, anonymous, reviewer(s) for their contribution to the peer review of this work.

**Publisher's note** Springer Nature remains neutral with regard to jurisdictional claims in published maps and institutional affiliations.

Springer Nature or its licensor (e.g. a society or other partner) holds exclusive rights to this article under a publishing agreement with the author(s) or other rightsholder(s); author self-archiving of the accepted manuscript version of this article is solely governed by the terms of such publishing agreement and applicable law.

© Springer Nature Limited 2025